Contents lists available at ScienceDirect

Transactions of Nonferrous Metals Society of China

36(2026) 600−613

www.tnmsc.cn

Effect of calcination temperature on interlayer spacing and oxygen vacancies concentration of $NaCu_{0.2}Fe_{0.3}Mn_{0.5}O_2$ layered materials for sodium-ion batteries

Bo-wen XU [a,b,c,#], Da ZHANG [a,b,c,#], Xuan-tian FENG [a,b,c], Sheng-ping HOU [a,b,c], Peng DONG [c,d,*], Dong-feng XUE [e], Feng LIANG [a,b,c,**]

[a] Key Laboratory for Nonferrous Vacuum Metallurgy of Yunnan Province, Kunming University of Science and Technology, Kunming 650093, China;

[b] National Engineering Research Center of Vacuum Metallurgy, Kunming University of Science and Technology, Kunming 650093, China;

[c] Faculty of Metallurgical and Energy Engineering, Kunming University of Science and Technology, Kunming 650093, China;

[d] National and Local Joint Engineering Laboratory for Lithium-Ion Batteries and Materials Preparation Technology, Kunming University of Science and Technology, Kunming 650093, China;

[e] Shenzhen Institute for Advanced Study, University of Electronic Science and Technology of China, Shenzhen 518110, China

Abstract: $NaCu_{0.2}Fe_{0.3}Mn_{0.5}O_2$ (NCFM) cathode material was synthesized using a simple solid-state reaction, and the effect of calcination temperature on its interlayer spacing and oxygen vacancies concentration was investigated. Through electrochemical testing and material characterizations, higher calcination temperatures increase the electrostatic repulsion between oxygen atoms in adjacent layers, resulting in an expansion of Na layer spacing. This structural change enhances the diffusion kinetics of Na^+, thereby significantly improving the rate performance of NCFM. Furthermore, elevated calcination temperatures facilitate the reduction of oxygen vacancies, leading to improved crystallinity. This enhancement in crystallinity mitigates structural strain during phase transitions, contributing to improved cyclic stability. Consequently, the optimized NCFM shows an initial discharge specific capacity of 143.3 mA·h/g at 0.1*C*, with a capacity retention rate of 79.28% after 100 cycles at 1*C*.

Keywords: sodium ion batteries; calcination temperature control; interlayer spacing; oxygen vacancies; electrochemical performance

1 Introduction

Lithium-ion batteries (LIBs) have become prevalent in high-power applications for consumer electronics and electric vehicles, primarily due to their superior electrochemical performance [1−3]. However, the limited and uneven distribution of Li reserves leads to elevated costs. In contrast, sodium-ion batteries (SIBs) utilize abundant and low-cost Na resources, exhibiting chemical properties similar to those of LIBs, thereby presenting a viable alternative for large-scale energy storage applications [4,5]. Over the past decade, a variety of cathode materials have been explored for SIBs, including transition metal (TM) layered oxides, polyanionic compounds,

# Bo-wen XU and Da ZHANG contributed equally to this work

Corresponding author: *Peng DONG, E-mail: dongpeng@kust.edu.cn;

**Feng LIANG, Tel: +86-15198797858, E-mail: liangfeng@kust.edu.cn

https://doi.org/10.1016/S1003-6326(25)66984-6

Received 28 May 2024; accepted 6 March 2025

and Prussian blue analogues. In particular, layered transition metal oxides (Na_xTMO_2, where TM represents Fe, Mn, Ni, Cu, Cr, etc.) are highly noticeable due to their high theoretical capacity, open framework, and facile synthesis [6−9].

Typically, Na_xTMO_2 compounds are generally categorized into two structural types (P2 and O3), where P and O represent prismatic and octahedral sites occupied by Na^+, respectively, and the latter number refers to the stacking period of TMO_2-layers in the cell unit [10−12]. The P2 phase exhibits superior cyclic stability and rate performance, attributed to the direct and rapid diffusion of Na^+ between the trigonal prismatic Na sites. However, its low initial coulombic efficiency (ICE) has hindered its widespread practical application [13]. Conversely, O3-phase cathode, which possesses adequate Na content, provides high power density. However, it is plagued by one or more complex phase transformations that occur due to Na^+ diffusion through the face-shared tetrahedral sites (intermediate sites) during the sodiation and desodiation processes, resulting in limited cycle stability and poor rate performance [14−17]. A common strategy to enhance electrochemical performance involves the optimization of the microscopic crystal structure. For example, LI et al [18] changed the lattice parameters of $Na_{0.7}Mn_{0.7}Ni_{0.3-x}Co_xO_2$ (x=0, 0.1, 0.3) by replacing Ni with Co, thus showing high-rate and cycling performance. WANG et al [19] found that replacing Fe or Mn element in $Na_{0.67}Mn_{0.5}Fe_{0.5}O_2$ with Al could increase the *d*-spacing and Na—O bond length of the material, which was more conducive to the diffusion of Na^+. Similarly, LI et al [20] partially introduced Al^{3+} into $NaFe_{1/3}Ni_{1/3}Mn_{1/3}O_2$ to reduce the lattice parameter *a* and thus enhance the structural stability. Although the introduction of heteroatoms into the parent phase can effectively modify the microscopic crystal structure of the material, the controllability of the crystal structure is highly sensitive to the elemental content and composition, which presents significant challenges for the precise synthesis of Na_xTMO_2. Furthermore, the doping process often necessitates additional procedural steps and increases material costs, thereby elevating both the complexity of the process and the overall preparation costs.

In contrast, the control of calcination temperature has been unequivocally demonstrated as an effective approach for the precise regulation of the structure of crystalline materials. However, research focusing the effects of calcination temperature control on the interlayer spacing and oxygen vacancies in Na_xTMO_2 crystals remains limited to date. Therefore, in this study, the effect of calcination temperature on the morphology, microstructure, crystallinity, and electrochemical performance of O3-phase $NaCu_{0.2}Fe_{0.3}Mn_{0.5}O_2$ (NCFM) cathode material was investigated. The interlayer spacing and oxygen vacancies of NCFM were assessed using various analytical techniques, and the mechanisms underlying crystal structural evolution were examined. The research results reveal a strong relationship between calcination temperature and both interlayer spacing and oxygen vacancies within the crystal structure. Furthermore, the effects of these parameters on electrode reaction kinetics, structural stability, and electrochemical performance were elucidated. These findings provide valuable insights and academic guidance for future structure modulation of sodium-ion O3-type layered cathode materials with high energy density and stability.

2 Experimental

2.1 Preparation of NCFM

Pure O3-phase layered metal oxides can be synthesized when the Cu/Fe/Mn molar ratio is maintained at 0.2∶0.3∶0.5 (Fig. S1 in Supporting Materials (SM)). The precursors utilized in this process include Fe_2O_3 (Macklin, 99 wt.%), Mn_2O_3 (Macklin, 99 wt.%), CuO (Macklin, 99 wt.%), and Na_2CO_3 (Macklin, 99.8 wt.%), which were combined through a simple solid-state reaction to prepare the samples. Subsequently, the mixed metallic oxide powders were subjected to grinding in a stainless-steel ball-milling pot at a rotation rate of 250 r/min for a duration of 15 h. Following uniform mixing, the powders were compacted into a pellet with a diameter of 16 mm under a pressure of 20 MPa. The resulting mixture was calcined at 450 °C for 6 h and then subjected to heating within the temperature range of 700−1000 °C (specifically at 700, 800, 900, and 1000 °C) for 15 h in an air atmosphere. These samples were designated as NCFM-700, NCFM-800, NCFM-900, and NCFM-1000, with the numerical designation corresponding to the calcination temperature (Fig. S2 in SM). It is noteworthy that Cu, Fe, and Mn, the key constituents

of NCFM, are plentiful in the Earth's crust and cheap to extract. This gives NCFM a low production cost advantage in the preparation process.

2.2 Electrochemical measurement

The electrochemical performance of the samples was investigated through the use of CR2032 coin batteries. The working electrodes were fabricated by casting a slurry composed of active material, acetylene black, and polyvinylidene fluoride (PVDF) binder in a mass ratio of 8∶1∶1, with N-methyl-2-pyrrolidone (NMP) serving as the solvent, onto aluminum foil. Subsequently, the working electrodes were subjected to drying at 80 °C in a vacuum for a duration of 10 h. The electrolyte consisted of a 1 mol/L $NaClO_4$ solution in a 1∶1 volume mixture of ethylene carbonate (EC) and diethyl carbonate (DEC), with the addition of 5 vol.% fluoroethylene carbonate (FEC). Pure Na foil was employed as the counter electrode, while porous glass fiber (GF/D) was utilized as the separator. Discharge and charge measurements and galvanostatic intermittent titration technique (GITT) were conducted using a Land CT2001A battery test system. Differential capacity curves (dQ/dV) are obtained by recording the voltage (V) and capacity (Q) data of the battery in constant current charge/discharge mode at the Land CT2001A battery test system [21]. During this process, a set of discrete voltage−capacity data points (V_i, Q_i) is collected. The capacity Q is calculated based on the following Eqs. (1) and (2):

$$Q = \int I\mathrm{d}t \tag{1}$$

where I is the charge/discharge current, and t is the time. By numerically differentiating the (V, Q) data, an approximation of dQ/dV can be obtained:

$$\mathrm{d}Q/\mathrm{d}V \approx (Q_{i+1}-Q_i)/(V_{i+1}-V_i) \tag{2}$$

Additionally, cyclic voltammetry (CV) of the electrode were performed using a CHI660E electrochemical station. The apparent diffusion efficiency of Na^+ can be calculated by Randles−Sevcik formula (Eq. (3)) [22]:

$$I_p = 2.69\times10^5 n^{2/3}\cdot A\cdot D^{1/2}\cdot v^{1/2}\cdot C_0 \tag{3}$$

where I_p is the peak current (mA), A is the effective area of the electrode (cm^2), D is the diffusion coefficient of Na^+ (cm^2/s), n is the electron transfer number of the electrode reaction, v is the sweep rate (V/s), and C_0 is the initial concentration of Na^+ in the lattice (mol/cm^3).

2.3 Characterization techniques

The morphology of the samples was investigated using scanning electron microscopy (SEM, ZEISS Supra 55). High-resolution transmission electron microscopy (HRTEM) images and energy-dispersive X-ray spectroscopy (EDS) mappings were obtained with a transmission electron microscope (TEM, JEM 2100F). X-ray diffraction (XRD) analysis was conducted using a diffractometer equipped with Cu K_α radiation (MXP3TA). The Rietveld method was employed to refine the raw XRD data of all samples, with the phase composition and lattice parameters data obtained through the GSASII software [23]. The refined data were subsequently utilized using the VESTA software to construct crystal structure models and obtain bond length data [24]. The precise chemical compositions of the synthesized cathode materials were determined through inductively coupled plasma optical emission spectrometry (ICP-OES, Agilent ICP-OES 720). Each sample was dissolved in 2 mL of aqua regia solution, which was then diluted with 2 vol.% HNO_3 prior to measurement. Raman spectra were recorded using a Renishaw In-Via Raman spectrometer with a laser wavelength of 488 nm. X-ray photoelectron spectroscopy (XPS) results, which included the identification of elemental types and their valence states, were characterized using a Thermo Scientific Nexsa Model K_α spectrometer equipped with Al K_α radiation (1486.68 eV). Thermal gravimetric analysis (TGA) of NCFM precursors was performed on a thermal analyzer (TGA/SDTA851e) at a heating rate of 5 °C/min in an air atmosphere. Fourier transform infrared spectroscopy (FTIR, FT/IR-660 Plus) data, corresponding to high spectral resolution, were obtained over a wide spectral range of 400−4000 cm^{-1}.

3 Results and discussion

3.1 Structural and morphology characterization of NCFM materials

As shown in Fig. 1, the phase composition of the products was analyzed using XRD. All samples exhibited diffraction peaks at 16.0°, 32.3°, 35.5°, 41.5°, 52.6°, and 57.2°, which can be accurately

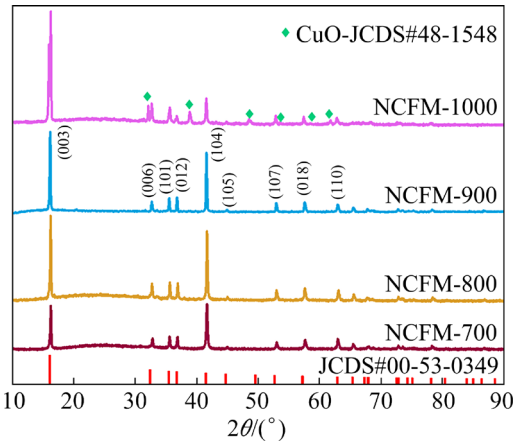

Fig. 1 XRD pattern of all NCFM samples

indexed to the (003), (006), (101), (104), (107) and (018) planes of the rhombohedral O3-phase structure (space group: *R*3*m*). In NCFM-1000 material, O3-phase structure was compromised, resulting in the formation of a significant amount of CuO impurity phases. This observation suggests that substantial structural disorder occurred in NCFM, preventing the attainment of a pure O3-phase at a calcination temperature of 1000 °C. Notably, the diffraction peak corresponding to the (003) plane of NCFM-900 is slightly shifted towards a lower Bragg angle in comparison to samples subjected to other calcination temperatures (Fig. S3 in SM), indicating a larger *d*-spacing of the (003) plane. In Fig. S4 in SM, the variation in *d*-spacing of the (003) crystal planes was corroborated by HRTEM. The *d*-spacing of NCFM-900 (5.48 Å) is greater than that of NCFM-800 (5.42 Å) and NCFM-700 (5.39 Å).

To elucidate the crystal structure, O3-phase configuration is illustrated in Fig. 2(a). In the O3-phase, the oxygen layers are arranged as ABCABC, and Na^+ and TM^{n+} occupy different octahedral sites, arranged in a face-centered cubic dense stack, with all Na sharing an edge and a face [25,26]. The lattice parameters were determined through a detailed analysis of XRD data utilizing Rietveld refinement method (Figs. 2(b−d) and Table S1 in SM). For all O3-phase samples, specifically NCFM-700, NCFM-800, and NCFM-900, the lattice parameter *a* decreases from 2.9499 (NCFM-700) to 2.9491 Å (NCFM-900), while the lattice parameter *c* increases

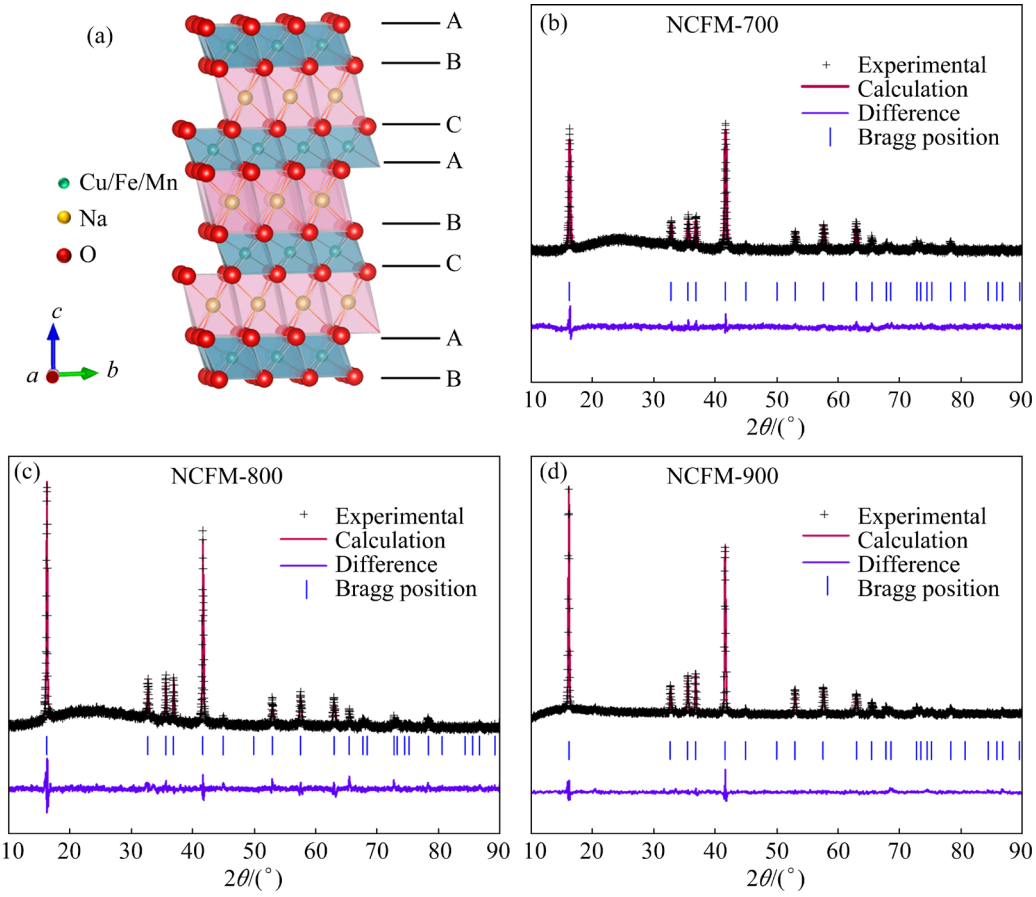

Fig. 2 Crystal structure of O3-phase NCFM (a), and Rietveld refinement XRD profiles of NCFM-700 (b), NCFM-800 (c) and NCFM-900 (d) samples

from 16.4053 (NCFM-700) to 16.4726 Å (NCFM-900), exhibiting an almost linear relationship with the increase in calcination temperature. Na—O bond length in NCFM-900 (2.3619 Å) is longer than that in NCFM-800 (2.3604 Å) and NCFM-700 (2.3576 Å). This trend suggests that as the calcination temperature rises, the covalent character of TM—O bonds increases, resulting in a decrease in the effective negative charge on O ions. Consequently, this leads to an elongated Na—O distance due to the diminished coulombic attraction between Na and O ions [27,28]. In addition, compared with NCFM-900, the XRD curves of NCFM-700 and NCFM-800 exhibit obvious broad peaks characteristic of a range of 20°−30°. This variation in peak characteristics is due to crystal structure defects and crystal size effects.

To investigate the effect of calcination temperature on the morphological characteristics of the samples, SEM images of the NCFM-700, NCFM-800, NCFM-900, and NCFM-1000 materials are depicted in Figs. 3(a−d), respectively. At a low calcination temperature of 700 °C, NCFM-700 displays a morphology characterized by the agglomeration of spherical primary particles. In contrast, at higher calcination temperatures of 800 and 900 °C, NCFM-800 and NCFM-900 exhibit flake- or brick-like morphologies. Upon further increasing the calcination temperature to 1000 °C, a significant number of cracks and fine particles were observed on the surface of NCFM-1000, indicating structural damage. Notably, NCFM-900 shows a large particle size within the pure O3-phase, suggesting that elevated calcination temperatures enhance the solid-phase diffusion rate during material synthesis [29]. In Fig. 3(e), EDS mapping images of NCFM-900 reveal a uniform distribution of Na, Cu, Fe, Mn, and O elements throughout the particles. Additionally, ICP-OES analysis of NCFM-900 was conducted to confirm TM content in the material (Table S2 in SM). The molar ratio of Na:Cu:Fe:Mn is approximately 0.999:0.201:0.299:0.489, which aligns with the anticipated design values of 1.0:0.2:0.3:0.5.

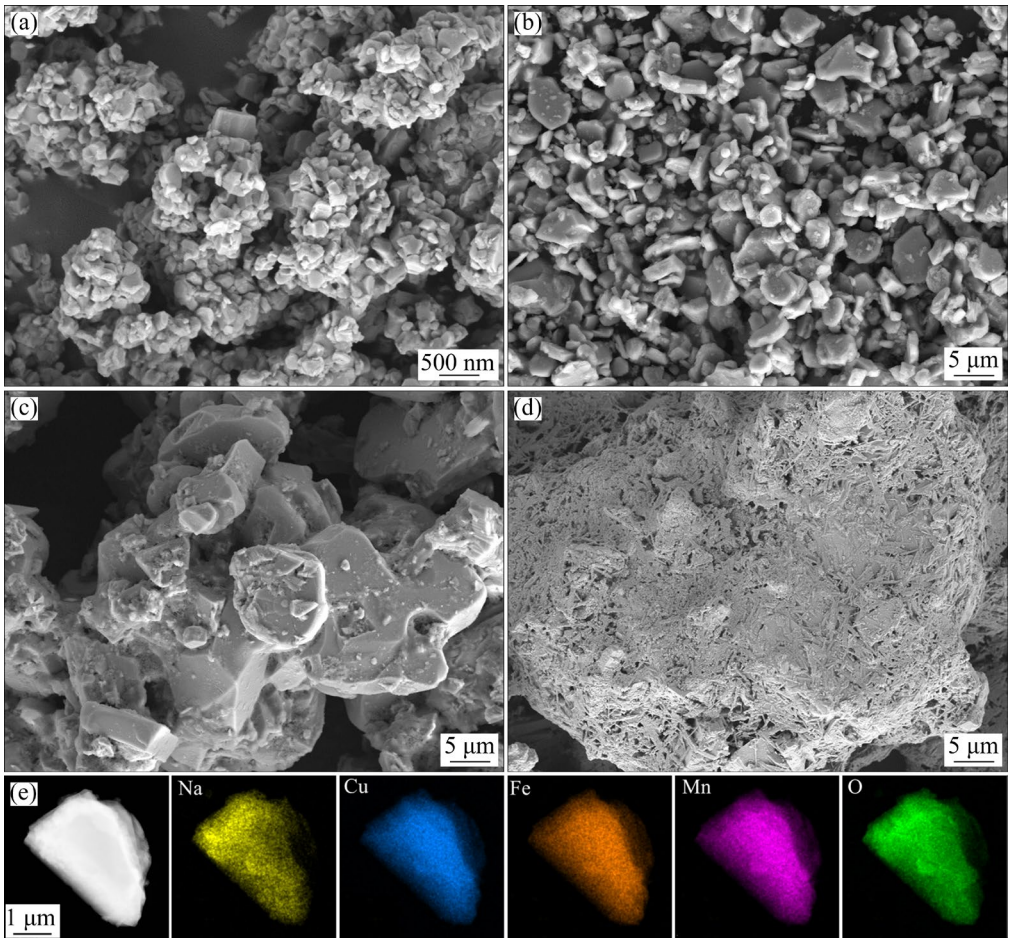

Fig. 3 SEM images of NCFM-700 (a), NCFM-800 (b), NCFM-900 (c) and NCFM-1000 (d) samples, and EDS mapping images of NCFM-900 sample (e)

The surface composition and elemental chemical states of NCFM materials were analyzed using XPS (Fig. 4). The survey spectra of NCFM materials reveal the presence of Na 1s, Mn 2p, Cu 2s, O 1s, and Auger peaks (Na KL1, Cu LM2, and O KL1) in Fig. 4(a). Notably, the absence of a signal corresponding to Fe element in the spectrogram suggests that iron is distributed within NCFM materials, a result that can be corroborated by EDS observations. The O 1s spectra exhibit characteristic peaks at approximately 529.4, 531.2, 532.8, and 535.6 eV, which are associated with Na_2CO_3, lattice oxygen, oxygen vacancy, and the Na Auger peak, respectively [30−32]. In Figs. 4(b−d), the concentration of oxygen vacancies in NCFM material and the Na_2CO_3 impurity on the surface diminishes with increasing calcination temperature. This trend indicates that higher calcination temperatures enhance crystallinity and reduce the structural defects of NCFM.

The chemical bonds of the prepared materials were studied using FTIR spectra and revealed in Fig. 5(a). Metal oxides generally give absorption bands below 1000 cm^{-1} arising from inter-atomic vibrations. For all NCFM samples, peaks observed at 866 and 430 cm^{-1} are attributed to TM—O bond vibration modes, while a peak at 1453 cm^{-1} confirms Na—O bond vibration [33,34]. The peaks were located at 1638 and 3441 cm^{-1} belonging to the O—H bending and O—H stretching vibrations of the moisture in the obtained material, respectively. Compared with NCFM-700 and NCFM-800, the peak intensity of TM—O and Na—O bonds in NCFM-900 is stronger, indicating a higher chemical bond homogeneity. This homogeneity contributes to a reduction in uneven stress distribution within NCFM-900 crystal, thereby enhancing the stability of its crystal structure. Similarly, detailed analysis on chemical bond characteristics of NCFM was provided by Raman spectra, as shown in Fig. 5(b). Raman peaks centered at approximately 485 and 591 cm^{-1}, characteristic of transition metal−oxygen bonds, correspond to $E1_g$ (O—TM—O bending) and $A1_g$ (TM—O stretching) vibrational modes, respectively. Furthermore, Raman peak at approximately 380 cm^{-1} is associated with the $E2_g$

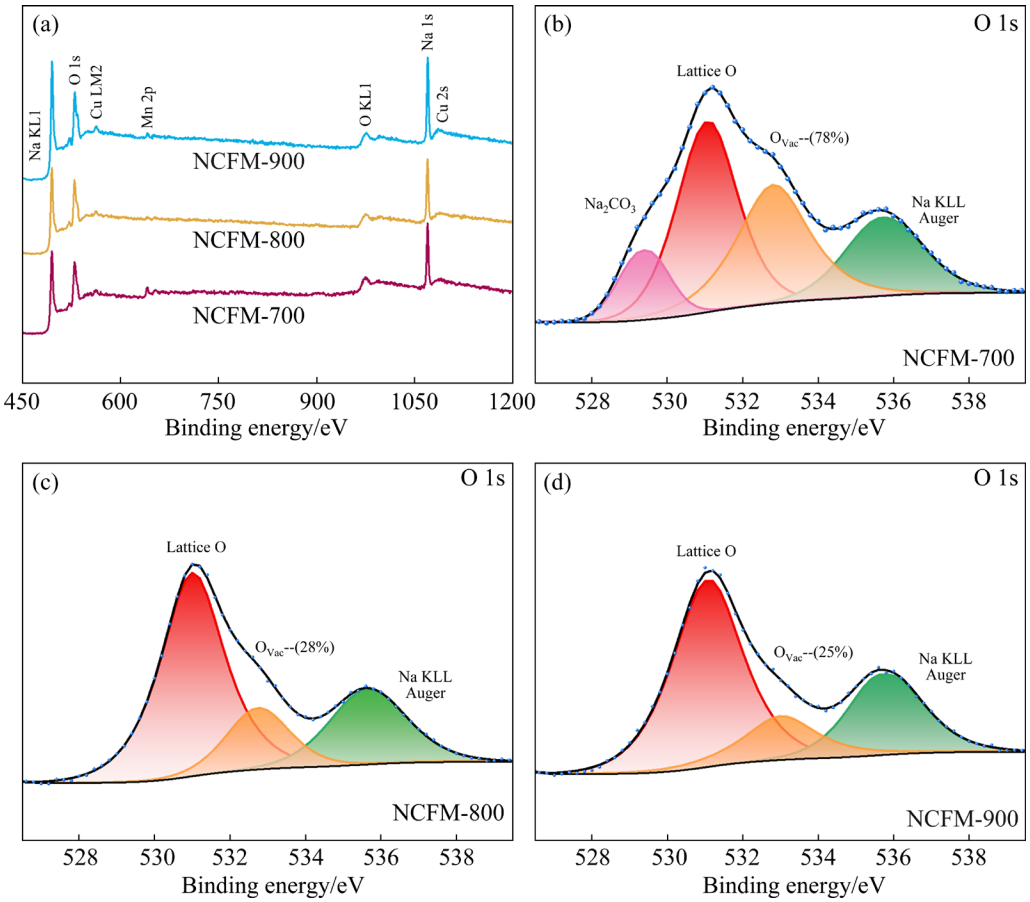

Fig. 4 XPS survey spectra of NCFM samples (a), and high-resolution O 1s XPS spectra of NCFM-700 (b), NCFM-800 (c) and NCFM-900 (d) samples

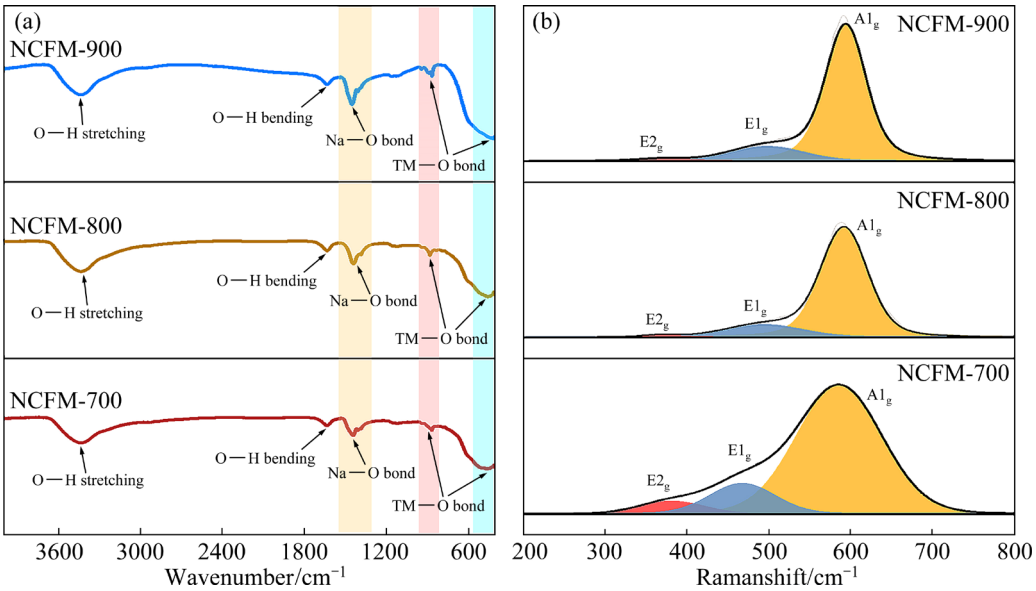

Fig. 5 FTIR spectra (a) and Raman spectra (b) of all samples

vibrations of Na—O [35,36]. As the calcination temperature increases, $A1_g$ peak pattern sharpens, indicating an enhancement in the crystallinity of NCFM. Importantly, the intensities of $E1_g$ and $E2_g$ peaks gradually diminish, while the intensity of $A1_g$ peak increases with rising calcination temperatures. This trend is closely linked to the enhancement of covalency in TM—O bonds and alteration in the interlayer spacing within the crystal structure.

3.2 Electrochemical performance

The electrochemical performances of NCFM-700, NCFM-800, and NCFM-900 cathodes were investigated using Na half-cells. CV curves for the three samples at a scan rate of 0.1 mV/s are illustrated in Fig. 6(a). NCFM-900 electrode exhibited a stronger peak current and a larger area of CV curve compared to NCFM-800 and NCFM-700 electrodes, indicating superior capacity storage performance [37]. Figure 6(b) depicts the initial galvanostatic charge/discharge profiles of the prepared batteries at a current density of 10 mA/g (0.1*C*). NCFM-900 cathode demonstrated the highest capacity of 92.5 mA·h/g, while NCFM-800 and NCFM-700 cathodes displayed lower discharge capacities of 88.6 and 60.8 mA·h/g, respectively. These results suggest that a higher calcination temperature facilitates the involvement of a greater number of Na^+ in the electrode reaction. In Fig. 6(c), the capacity retention rates of NCFM-900, NCFM-800, and NCFM-700 cathodes after 100 cycles are 79.28%, 72.83%, and 50.50% (1*C*), respectively. The primary factors contributing to the capacity decline of NCFM include the formation of chemical−electrochemical interfaces, which increase battery impedance, and the gradual collapse of the layered structure due to the repeated sodiation/desodiation of Na^+, leading to structural disintegration. As shown in Figs. 6(d) and S5 in SM, the dQ/dV analysis shows that the peak position of NCFM-900 cathode changes (25 mV) less than that of NCFM-800 (62 mV) and NCFM-700 (73 mV) cathodes. This indicates that the higher crystallinity NCFM-900 material exhibits better structural stability, resulting in effective mitigation of structural strain during the phase transition process.

To further investigate the effect of calcination temperature on the electrochemical performance of NCFM, charge/discharge tests were performed over a wider voltage range (2−4.2 V). As shown in Fig. 7(a), the initial discharge capacities of NCFM were found to increase with rising calcination temperatures, yielding values of 143.3, 125.3, and 58.4 mA·h/g for NCFM-900, NCFM-800, and NCFM-700, respectively. Additionally, NCFM-900 cathode exhibited the highest ICE at 97.3%. This enhancement is attributed to the participation of manganese in the redox reactions occurring within the voltage range of 2−4.2 V, which activates a great number of active sites [38]. This further indicates that NCFM-900 possesses superior structural stability, enabling it to withstand the structural alterations induced by the extraction and insertion of excess Na^+. Besides the difference in discharge

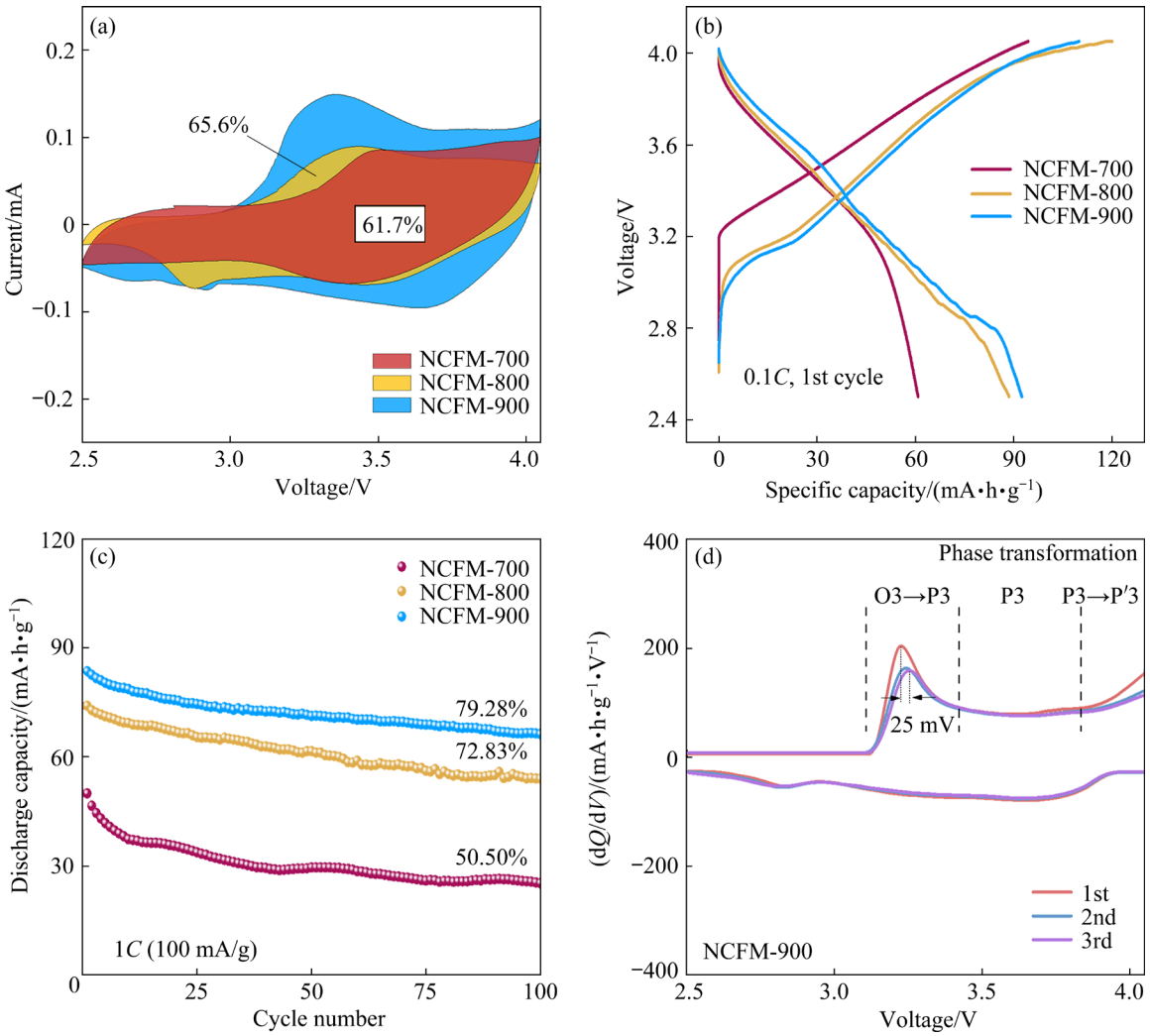

Fig. 6 (a) CV curves of NCFM at scan rate of 0.1 mV/s; (b) Charge/discharge curves of NCFM (1*C*=100 mA/g); (c) Cycling performance of NCFM at 1*C* within 2.5−4.05 V; (d) d*Q*/d*V* curves of NCFM-900 at different cycles

capacity and ICE, the specific energy density of NCFM-900 cathode is higher than that of NCFM-800 and NCFM-700 (Fig. 7(b)). This result further confirms that the electrochemical performance of NCFM is significantly optimized with elevated calcination temperature. In addition, the reversible capacities of NCFM-900 cathode at all tested current densities exceed those of NCFM-800 and NCFM-700 (Figs. 7(c) and S6). Specifically, the capacities of NCFM-900 cathode were 143.3, 127, 111.3, 96.0, and 80.2 mA·h/g at current rates of 0.1*C*, 0.2*C*, 0.5*C*, 1*C*, and 2*C*, respectively. These correspond to capacity retention rates of 88.62%, 77.66%, 66.99%, and 55.96% of the initial reversible capacity. The improved rate performance is attributed to the increased Na layer spacing resulting from higher calcination temperatures (700−900 °C). This result also suggests that the ion diffusion channel has become the limiting factor for Na^+ diffusion rates in NCFM, as opposed to the ion migration distance. Figure 7(d) depicts the cycling performance of NCFM-900 at 0.2*C*. The initial discharge of NCFM-900 is recorded at 130.7 mA·h/g, which decreases to 106.4 mA·h/g after 40 cycles, resulting in a capacity retention of 81.2%. The d*Q*/d*V* curve, obtained through differential analysis of the discharge curves, delineates the dynamic characteristics of NCFM-900 during the discharge process (Fig. S7 in SM). The d*Q*/d*V* curves reveal a reduction peak for Mn^{4+}/Mn^{3+} near 2.2 V, indicating that manganese in NCFM contributes to charge compensation across a wide voltage range (2−4.2 V), thereby facilitating a higher discharge capacity [39,40]. According to the above, NCFM-900 demonstrates superior electrochemical performance, primarily attributable to its enhanced crystallinity and the increased Na layer spacing.

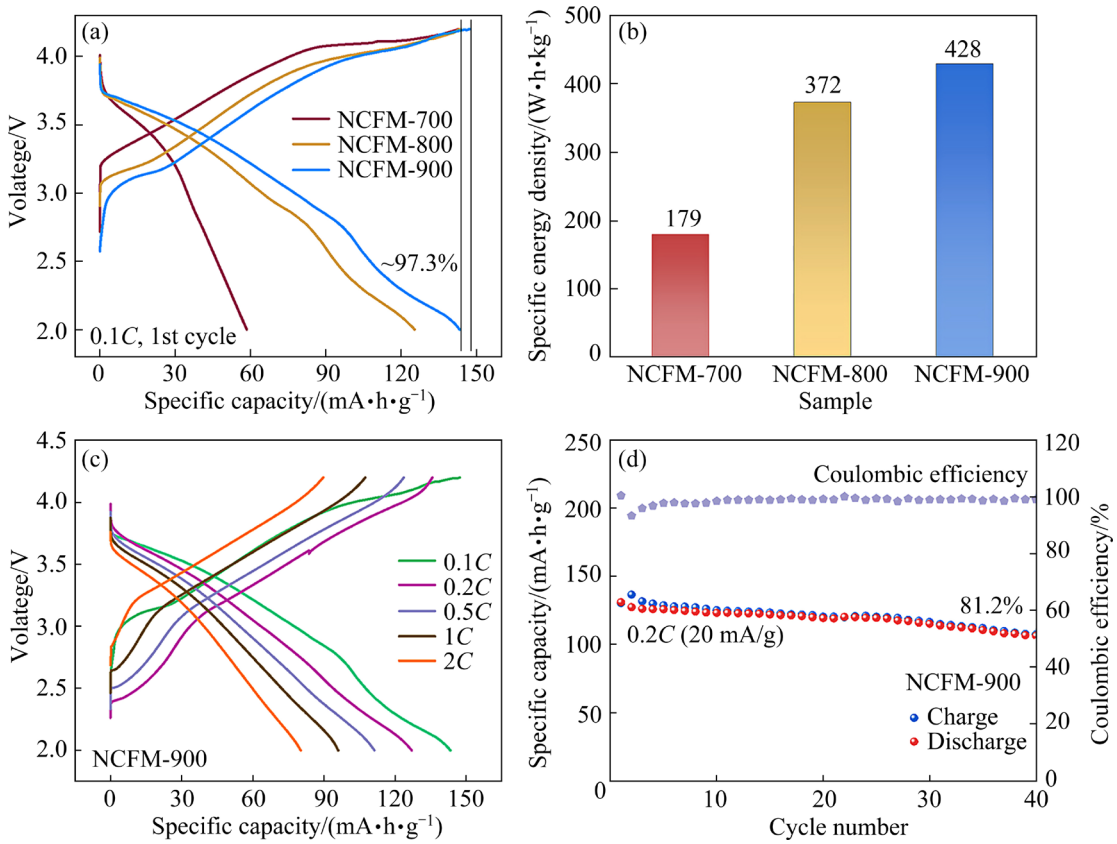

Fig. 7 (a) Charge/discharge profiles of NCFM at 0.1*C* within 2−4.2 V; (b) Energy density of NCFM within 2−4.2 V; (c) Rate performance of NCFM-900; (d) Cycling performance of NCFM-900 at 0.2*C* within 2−4.2 V

3.3 Electrode process kinetics

To explore the effect of calcination temperature on the kinetic behavior of Na in NCFM, CV curves were obtained at various sweep rates, with the corresponding line fitting results in Figs. 8(a, b) and S8 in SM. NCFM-900 electrode demonstrated a higher apparent diffusion efficiency for Na compared to NCFM-700 and NCFM-800 electrodes. Additionally, the kinetics of Na^+ diffusion were further analyzed using GITT. Utilizing Eq. (4) proposed by WEPPNER and HUGGINS [41], apparent diffusion coefficient of Na^+ (D_{Na}) during the second charge/discharge cycle is determined as follows:

$$D=\frac{4}{\pi\tau}\left(\frac{m_B V_m}{M_B S}\right)^2\left(\frac{\Delta E_S}{\Delta E_\tau}\right)^2 \quad (4)$$

where D is the apparent diffusion coefficient; τ means the applied current time interval; m_B, V_m, and M_B represent the mass of active material, molecular volume, and molar mass, respectively; S refers to the electrode effective surface area, which was calculated from the electrode properties and the average particle size; ΔE_S and ΔE_τ respectively are changes in the steady-state voltage and total change of the battery voltage during each GITT step (Fig. 8(c)). D_{Na} determined from GITT curves (Figs. 8(d) and S9 in SM), plotted against state of charge (SoC) during both sodiation and desodiation, is presented in Figs. 8(e, f). The profiles of NCFM-800 and NCFM-900 exhibit similar trends, with distinct troughs observed during both the charging and discharging processes, suggesting that these samples undergo comparable phase transitions and structural rearrangements. Notably, NCFM-900 cathode shows a higher D_{Na} value throughout most of the sodiation and desodiation processes compared to both NCFM-700 and NCFM-800. Specifically, D_{Na} for NCFM-900 increases from an initial value of 2.27×10^{-11} cm^2/s, reaching a maximum of 2.96×10^{-11} cm^2/s at approximately 59% SoC, followed by a gradual decrease. During discharge, two peaks are observed at 2.82×10^{-11} and 3.57×10^{-11} cm^2/s at approximately 59% and 98% SoC, respectively. Additionally, the average D_{Na} for

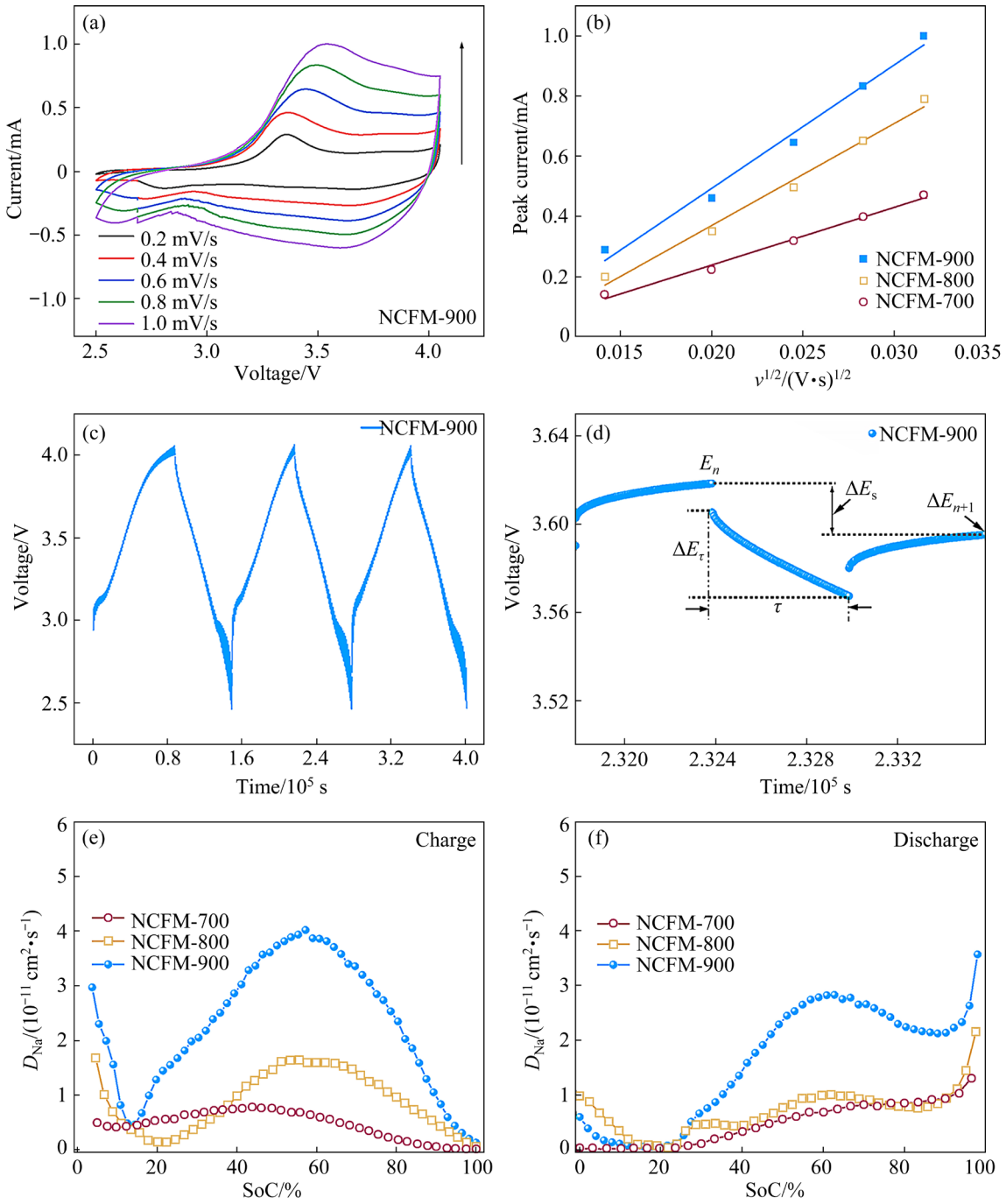

Fig. 8 (a) CV curves of NCFM-900 at different sweep rates; (b) Peak current as function of square root for scan rate ($v^{1/2}$); (c) Schematic of single current pulse for GITT; (d) GITT curves of NCFM-900 cathode in the second cycle within 2.5−4.05 V; (e, f) Calculated Na^+ diffusion efficiency vs SoC

NCFM-900 is calculated to be 2.28×10^{-11} cm^2/s during the charge process and 1.60×10^{-11} cm^2/s during the discharge process (Fig. S10 in SM). These values are significantly higher than those of NCFM-800 and NCFM-700, which further confirms that the increased calcination temperature is favorable to widen the ion diffusion channel, thus promoting the fast diffusion of Na^+.

3.4 Structure evolution mechanism

Figure 9 illustrates the morphological and crystallographic changes in O3-phase NCFM samples subjected to varying calcination temperatures. NCFM samples maintain a consistent O3-phase structure at calcination temperatures of 700, 800, and 900 °C. However, as the calcination temperature increases, the morphology transitions

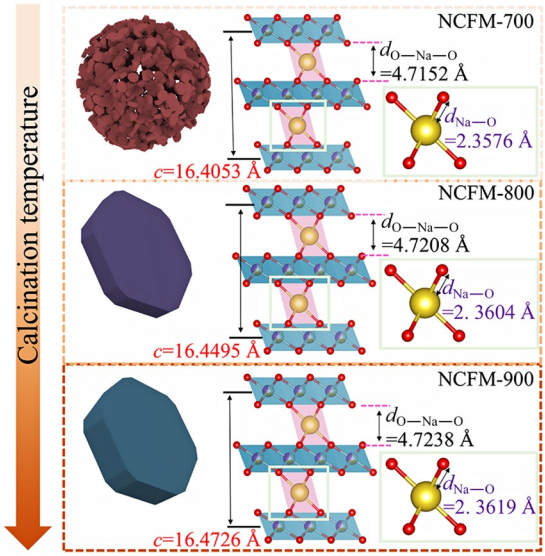

Fig. 9 Morphological and crystal structure changes of O3-phase NCFM samples at different calcination temperatures

from a spherical agglomeration of primary particles to a flake-like structure, and with further elevation in temperature, it evolves into a brick-like morphology. This indicates that elevated calcination temperatures enhance solid-phase diffusion rates during the synthesis of the material, thereby promoting the particle growth. Additionally, higher calcination temperatures contribute to improved chemical bonding homogeneity and reduction of oxygen vacancies within NCFM structure. Such changes can mitigate structural strain during the phase transformation process to a certain degree, thereby enhancing the structural stability of NCFM samples. As the calcination temperature increases, the covalency of TM—O bonds in NCFM is enhanced and the coulombic attraction between Na and O ions is suppressed. This leads to an increase in the electrostatic repulsion between oxygen atoms in adjacent layers of the crystal structure, thereby causing the interlayer spacing to increase. When the calcination temperature increases from 700 to 900 °C, the length of Na—O bond is increased from 2.3576 to 2.3619 Å, and the interlayer spacing of NCFM expands from 4.7152 to 4.7238 Å. This crystal structure change can promote the fast diffusion of Na^+ in NCFM materials during charging and discharging, thereby improving the rate performance of NCFM. Therefore, NCFM-900 with fewer oxygen vacancies and larger Na layer spacing shows better electrochemical performance.

4 Conclusions

(1) NCFM cathode materials were synthesized using the solid-phase reaction method, with their crystal structure and crystallinity optimized through calcination temperature adjustments.

(2) Calcination temperature is crucial in improving the electrochemical performance of NCFM. Higher calcination temperatures result in expanded layer spacing and reduced oxygen vacancies within the crystal structure, thereby enhancing rate performance and cycling stability.

(3) An initial discharge specific capacity of 143.3 mA·h/g was achieved at 0.1*C*, with a capacity retention of 79.28% after 100 cycles at 1*C*. Even at elevated rates (2*C*), the discharge specific capacity remained stable, exceeding 80.2 mA·h/g.

(4) Electrochemical properties and reaction mechanisms were conducted using various electrochemical techniques. Studies of charge/discharge test, CV, and GITT indicate that NCFM-900 demonstrates superior kinetic properties.

(5) A thorough assessment of the structural evolution of NCFM across different calcination temperatures was performed, developing a foundation for developing effective methods to synthesize O3-phase layered cathode materials with high energy density and stability.

CRediT authorship contribution statement

Bo-wen XU: Conceptualization, Methodology, Investigation, Writing – Original draft, Review & editing; **Da ZHANG:** Conceptualization, Methodology; **Xuan-tian FENG:** Conceptualization, Methodology; **Sheng-ping HOU:** Investigation; **Peng DONG:** Investigation; **Dong-feng XUE:** Investigation; **Feng LIANG:** Investigation.

Declaration of competing interest

The authors declare that they have no known competing financial interests or personal relationships that could have appeared to influence the work reported in this paper.

Acknowledgments

The work was supported by the National Natural Science Foundation of China (No. 12175089), the Key Research and Development Program of Yunnan Province, China (No. 202103AF140006), Basic Research Programs

of Yunnan Provincial Science and Technology Department, China (Nos. 202001AW070004, 202301AS070051, 202401AV070008), Yunnan Industrial Innovative Talents Program for "Xingdian Talent Support Plan", China (No. KKXY202252001), and Yunnan Major Scientific and Technological Projects, China (No. 202202AG050003).

Supporting Materials

Supporting Materials in this paper can be found at: https://tnmsc.csu.edu.cn/download/17-p0600-2024-0762-Supporting_Materials.pdf.

References

[1] LI Fang-cheng, ZHANG Gang, ZHANG Zong-liang, YANG Jian, LIU Fang-yang, JIA Ming, JIANG Liang-xing. Regeneration of Al-doped $LiNi_{0.5}Co_{0.2}Mn_{0.3}O_2$ cathode material by simulated hydrometallurgy leachate of spent lithium-ion batteries [J]. Transactions of Nonferrous Metals Society of China, 2022, 32(2): 593−603.

[2] ZENG Jing, PENG Chao-qun, WANG Ri-chu, LIU Ya-jing, WANG Xiao-feng, LIU Jun. Preparation of dual-shell Si/TiO_2/CFs composite and its lithium storage performance [J]. Transactions of Nonferrous Metals Society of China, 2019, 29(11): 2384−2391.

[3] SHRAER S, DEMBITSKIY A, TRUSSOV I, KOMAYKO A, AKSYONOV D, LUCHININ N, MOROZOV A, POLLASTRI S, AQUILANTI G, RYAZANTSEV S, NIKITINA V, ABAKUMOV A, ANTIPOV E, FEDOTOV S. Designing a 3D framework $NaVOPO_4$ as a high-power, low-strain and long-life positive electrode material for Na-ion batteries [J]. Energy Storage Materials, 2024, 68: 103358.

[4] YANG Huan, WANG Dong, LIU Ya-lan, LIU Yi-hua, ZHONG Ben-he, SONG Yang, KONG Qing-quan, WU Zhen-guo, GUO Xiao-dong. Improvement of cycle life for layered oxide cathodes in sodium-ion batteries [J]. Energy & Environmental Science, 2024, 17(5): 1756−1780.

[5] QIN Mu-lan, LIU Wan-min, XIANG Yuan-jin, WANG Wei-gang, SHEN Bin. Synthesis and electrochemical performance of V_2O_5/NaV_6O_{15} nanocomposites as cathode materials for sodium-ion batteries [J]. Transactions of Nonferrous Metals Society of China, 2020, 30(8): 2200−2206.

[6] WANG Xuan-peng, XIAO Zhi-tong, HAN Kang, ZHANG Xiao, LIU Ziang, YANG Chen, MENG Jia-shen, LI Ming, HUANG Meng, WEI Xiu-juan, MAI Li-qiang. Advances in fine structure optimizations of layered transition-metal oxide cathodes for potassium-ion batteries [J]. Advanced Energy Materials, 2023, 13(2): 2202861.

[7] CHENG Lei, ZHAO Yi, HUANG Bin, ZHAO Zao-wen, LI Yan-wei, LI Wei. Effects of W-doping on precursor growth of $LiNi_{0.88}Co_{0.09}Mn_{0.03}O_2$ and its electrochemical performance [J]. Transactions of Nonferrous Metals Society of China, 2024, 34(4): 1251−1262.

[8] LI Fei, LIU Ren-bin, LIU Jie, LI Hong-sen. Voltage hysteresis in transition metal oxide cathodes for Li/Na-ion batteries [J]. Advanced Functional Materials, 2023, 33(28): 2300602.

[9] HUANG Han-jiao, WU Xiao-wei, GAO Yan-jun, LI Zong-you, WANG Wei, DONG Wen-shuai, SONG Qing-yi, GAN Song-jie, ZHANG Jian-guo, YU Qi-yao. Polyanionic cathode materials: A comparison between Na-ion and K-ion batteries [J]. Advanced Energy Materials, 2024, 14(14): 2304251.

[10] QIN Mu-lan, YIN Chang-yu, XU Wen, LIU Yang, WEN Jun-hao, SHEN Bin, WANG Wei-gang, LIU Wan-min. Facile synthesis of high capacity P2-type $Na_{2/3}Fe_{1/2}Mn_{1/2}O_2$, cathode material for sodium-ion batteries [J]. Transactions of Nonferrous Metals Society of China, 2021, 31(7): 2074−2080.

[11] ZUO Wen-hua, QIU Ji-min, LIU Xiang-si, REN Fu-cheng, LIU Hao-dong, HE Hua-jin, LUO Chong, LI Jia-lin, ORTIZ F G, DUAN Hua-nan, LIU Jin-ping, WANG Ming-sheng, LI Yang-xing, FU Ri-qiang, YANG Yong. The stability of P2-layered sodium transition metal oxides in ambient atmospheres [J]. Nature Communications, 2020, 11(1): 3544.

[12] DING Yu-qing, WANG Shi-min, SUN Yong-jiang, LIU Qing, AN Qi, GUO Hong. Layered cathode-$Na_{0.67}Li_{0.15}Ni_{0.18}Mg_{0.02}$-$Mn_{0.8}O_2$ with P2/O3 hybrid phase for high-performance Na-ion batteries [J]. Journal of Alloys and Compounds, 2023, 939: 168780.

[13] CHENG Zhi-wei, ZHAO Bin, GUO Yu-jie, YU Lian-zheng, YUAN Bo-heng, HUA Wei-bo, YIN Ya-xia, XU Sai-long, XIAO Bing, HAN Xiao-gang, WANG Peng-fei, GUO Yu-guo. Mitigating the large-volume phase transition of P2-type cathodes by synergetic effect of multiple ions for improved sodium-ion batteries [J]. Advanced Energy Materials, 2022, 12(14): 2103461.

[14] WANG Peng-fei, YAO Hu-rong, LIU Xin-yu, ZHANG Jie-nan, GU Lin, YU Xi-qian, YIN Ya-xia, GUO Yu-guo. Ti-substituted $NaNi_{0.5}Mn_{0.5-x}Ti_xO_2$ cathodes with reversible O3-P3 phase transition for high-performance sodium-ion batteries [J]. Advanced Materials, 2017, 29(19): 1700210.

[15] LI Ran-ran, GAO Jian, LI Jun-peng, HUANG Hao, LI Xiao-lei, WANG Wen-long, ZHENG Li-rong, HAO Shu-meng, QIU Jie-shan, ZHOU Wei-dong. An undoped tri-phase coexistent cathode material for sodium-ion batteries [J]. Advanced Functional Materials, 2022, 32(41): 2205661.

[16] PENG Jian, HUANG Jia-qi, GAO Yun, QIAO Yun, DONG Huan-huan, LIU Yang, LI Li, WANG Jia-zhao, DOU Shi-xue, CHOU Shu-lei. Defect-healing induced monoclinic iron-based Prussian blue analogs as high-performance cathode materials for sodium-ion batteries [J]. Small, 2023, 19(36): 2300435.

[17] ZHANG Hang, GAO Yun, LIU Xiao-hao, ZHOU Li-feng, LI Jia-yang, XIAO Yao, PENG Jian, WANG Jia-zhao, CHOU Shu-lei. Long-cycle-life cathode materials for sodium-ion batteries toward large-scale energy storage systems [J]. Advanced Energy Materials, 2023, 13(23): 2300149.

[18] LI Zheng-yao, ZHANG Ji-cheng, GAO Rui, ZHANG Heng, HU Zhong-bo, LIU Xiang-feng. Unveiling the role of Co in improving the high-rate capability and cycling performance of layered $Na_{0.7}Mn_{0.7}Ni_{0.3-x}Co_xO_2$ cathode materials for sodium-ion batteries [J]. ACS Applied Materials & Interfaces, 2016, 8(24): 15439−15448.

[19] WANG Hui-bo, GAO Rui, LI Zheng-yao, SUN Li-mei, HU Zhong-bo, LIU Xiang-feng. Different effects of Al

substitution for Mn or Fe on the structure and electrochemical properties of $Na_{0.67}Mn_{0.5}Fe_{0.5}O_2$ as a sodium ion battery cathode material [J]. Inorganic Chemistry, 2018, 57(9): 5249−5257.

[20] LI Xiao-wei, SHEN Xing, ZHAO Jun-mei, YANG Yang, ZHANG Qiang-qiang, DING Fei-xiang, HAN Miao, XU Chun-liu, YANG Chao, LIU Hui-zhou, HU Yong-sheng. O3-$NaFe_{(1/3-x)}Ni_{1/3}Mn_{1/3}Al_xO_2$ cathodes with improved air stability for Na-ion batteries [J]. ACS Applied Materials & Interfaces, 2021, 13(28): 33015−33023.

[21] HAN Xue-bing, OUYANG Ming-gao, LU Lan-guang, LI Jian-qiu, ZHENG Yue-jiu, LI Zhe. A comparative study of commercial lithium ion battery cycle life in electrical vehicle: Aging mechanism identification [J]. Journal of Power Sources, 2014, 251(1): 38−54.

[22] DONG Rui-qi, ZHENG Lu-min, BAI Ying, NI Qiao, LI Yu, WU Feng, REN Hai-xia, WU Chuan. Elucidating the mechanism of fast Na storage kinetics in ether electrolytes for hard carbon anodes [J]. Advanced Materials, 2021, 33(36): 2008810.

[23] TOBY B H, von DREELE R B. GSAS-II: The genesis of a modern open-source all purpose crystallography software package [J]. Journal of Applied Crystallography, 2013, 46(2): 544−549.

[24] MOMMA K, IZUMI F. VESTA 3 for three-dimensional visualization of crystal, volumetric and morphology data [J]. Journal of Applied Crystallography, 2011, 44(6): 1272−1276.

[25] PANG Jian, KONG Ling-xin, ZHU Li-guo, XU Bao-qiang, XU Jun-jie, BAI Chong-lin, YANG Bin. Preparation of ultralow-oxygen titanium by direct reduction of TiO_2 [J]. Transactions of Nonferrous Metals Society of China, 2024, 34(2): 681−693.

[26] WU Lin-rong, ZHANG Yu-han, WU Zhen, TIAN Jin-lv, WANG Hao-rui, ZHAO Hai-jun, XU Shou-dong, CHEN Liang, DUAN Xiao-chuan, ZHANG Ding, GUO Hui-juan, YOU Ya, ZHU Zhi. Stabilized O3-type layered sodium oxides with enhanced rate performance and cycling stability by dual-site Ti^{4+}/K^+ substitution [J]. Advanced Science, 2023, 10(32): 2304067.

[27] KUMAR B S, PRADEEP A, SRIHARI V, POSWAL H K, KUMAR R, AMARDEEP A, CHATTERJEE A, MUKHOPADHYAY A. Cation-oxygen bond covalency: A common thread and a major influence toward air/water-stability and electrochemical behavior of “layered” Na-transition-metal-oxide-based cathode materials [J]. Advanced Energy Materials, 2023, 13(19): 2204407.

[28] WANG Yao, ZHAO Xu-dong, JIN Jun-teng, SHEN Qiu-yu, HU Yang, SONG Xiao-bai, LI Han, QU Xuan-hui, JIAO Li-fang, LIU Yong-chang. Boosting the reversibility and kinetics of anionic redox chemistry in sodium-ion oxide cathodes via reductive coupling mechanism [J]. Journal of the American Chemical Society, 2023, 145(41): 22708−22719.

[29] XU Hao, ZHANG Chun-mei, CAI Jing-xuan, WANG Jia, LIU Kai-qiang, CHENG Xiao-wei. Synthesis and characterization of activated alumina with high thermal stability by a low-heat solid-phase precursor method [J]. Microporous and Mesoporous Materials, 2022, 337: 111921.

[30] SHEN Qiu-yu, LIU Yong-chang, ZHAO Xu-dong, JIN Jun-teng, WANG Yao, LI Sheng-wei, LI Ping, QU Xuan-hui, JIAO Li-fang. Transition-metal vacancy manufacturing and sodium-site doping enable a high-performance layered oxide cathode through cationic and anionic redox chemistry [J]. Advanced Functional Materials, 2021, 31(51): 2106923.

[31] LIN Chen-han, MENG Xiang-cong, LIANG Min, LI Wen-ya, LIANG Jin-ji, LIU Teng-fei, KE Xi, LIU Jun, SHI Zhi-cong, LIU Li-ying. Facilitating reversible transition metal migration and expediting ion diffusivity via oxygen vacancies for high performance O3-type sodium layered oxide cathodes [J]. Journal of Materials Chemistry A, 2023, 11(1): 68−76.

[32] XU Bo-wen, ZHANG Da, CHANG Shi-lei, HOU Min-jie, PENG Chao, XUE Dong-feng, YANG Bin, LEI Yong, LIANG Feng. Fabrication of long-life quasi-solid-state $Na-CO_2$ battery by formation of $Na_2C_2O_4$ discharge product [J]. Cell Reports Physical Science, 2022, 3(7): 100973.

[33] GAN Lu, YUAN Xin-guang, HAN Jia-jun, YANG Xi-nan, ZHENG Li-tuo, HUANG Zhi-gao, YAO Hu-rong. Highly symmetrical six-transition metal ring units promising high air-stability of layered oxide cathodes for sodium-ion batteries [J]. Advanced Functional Materials, 2023, 33(7): 2209026.

[34] CHAALI Y, DAHBI M, SABBAR E, ZAKARIA D. Comparative study of $Na_{0.67}Ni_{0.25}Co_{0.17}Mn_{0.58}O_2$ P-Type cathode materials for sodium-ion batteries: Combustion synthesis and combined analysis of structural, electrical, and dielectric properties [J]. Ceramics International, 2023, 49(21): 33607−33617.

[35] KALYONCUOGLU B, OZGUL M, ALTUNDAG S, BULUT F, OZ E, SAHINBAY S, ALTIN S. High-performance Na-ion full-cells with P2-type $Na_{0.67}Mn_{0.5-x}Ni_x-Fe_{0.43}Al_{0.07}O_2$ cathodes: Cost analysis for stationary battery storage systems [J]. Journal of Energy Storage, 2024, 79: 110203.

[36] CAI Tian-xun, CAI Ming-zhi, MU Jin-xiao, ZHAO Si-wei, BI Hui, ZHAO Wei, DONG Wu-jie, HUANG Fu-qiang. High-entropy layered oxide cathode enabling high-rate for solid-state sodium-ion batteries [J]. Nano-Micro Letters, 2024, 16(1): 10.

[37] XIA Ji-li, YAN Dong, GUO Li-ping, DONG Xiao-ling, LI Wen-cui, LU An-hui. Hard carbon nanosheets with uniform ultramicropores and accessible functional groups showing high realistic capacity and superior rate performance for sodium-ion storage [J]. Advanced Materials, 2020, 32(21): 2000447.

[38] WEI Ting-ting, LIU Xu, YANG Shao-Jie, WANG Peng-fei, YI Ting-feng. Regulating the electrochemical activity of Fe-Mn-Cu-based layer oxides as cathode materials for high-performance Na-ion battery [J]. Journal of Energy Chemistry, 2023, 80: 603−613.

[39] LV Zhuo-ran, PENG Bai-xin, LV Xi-meng, GAO Yu-sha, HU Ke-yan, DONG Wu-jie, ZHENG Geng-feng, HUANG Fu-qiang. Intercalative motifs-induced space confinement and bonding covalency enhancement enable ultrafast and large sodium storage [J]. Advanced Functional Materials, 2023, 33(16): 2214370.

[40] HU Bei, QIU Qing, LI Chao, SHEN Ming, HU Bing-wen, TONG Wei, WANG Kun-chan, ZHOU Qing-ping, ZHANG Yan-ming, HE Zhi-an, ZHANG Teng, CHEN Chang-xin. Tailoring anionic redox activity in a P2-type sodium layered oxide cathode via Cu substitution [J]. ACS Applied Materials & Interfaces, 2022, 14(25): 28738−28747.

[41] WEPPNER W, HUGGINS R A. Electrochemical investigation of the chemical diffusion, partial ionic conductivities, and other kinetic parameters in Li_3Sb and Li_3Bi [J]. Journal of Solid State Chemistry, 1977, 22(3): 297−308.

煅烧温度对钠离子电池 $NaCu_{0.2}Fe_{0.3}Mn_{0.5}O_2$ 层状材料层间距和氧空位浓度的影响

许博文[1,2,3]，张 达[1,2,3]，冯宣天[1,2,3]，侯圣平[1,2,3]，董 鹏[3,4]，薛冬峰[5]，梁 风[1,2,3]

1. 昆明理工大学 有色金属真空冶金云南省重点实验室，昆明 650093；
2. 昆明理工大学 真空冶金国家工程研究中心，昆明 650093；
3. 昆明理工大学 冶金与能源工程学院，昆明 650093；
4. 昆明理工大学 锂离子电池与材料制备技术国家与地方联合工程实验室，昆明 650093；
5. 电子科技大学 深圳高等研究院，深圳 518110

摘 要：采用简单的固相法合成了 $NaCu_{0.2}Fe_{0.3}Mn_{0.5}O_2$(NCFM)正极材料，并研究了煅烧温度对其层间距和氧空位浓度的影响。通过电化学测试和材料表征发现，较高的煅烧温度增加了相邻层中氧原子之间的静电排斥力，从而导致 Na 层间距扩大。这种结构变化增强了 Na^+的扩散动力学，显著提高了 NCFM 的倍率性能。此外，煅烧温度的升高有利于减少氧空位缺陷，提高结晶度。结晶度的增强缓解了相变过程中的结构应变，有助于提高循环稳定性。因此，优化后的 NCFM 在 0.1*C* 倍率时的初始放电比容量为 143.3 mA·h/g，在 1*C* 倍率下循环 100 次后的容量保持率为 79.28%。

关键词：钠离子电池；煅烧温度控制；层间距；氧空位；电化学性能

(Edited by Xiang-qun LI)